Effect of heat treatment on the microstructure characteristics and microhardness of a novel γ′ nickel-based superalloy by laser powder bed

Results in Materials 12 (2021) 100232

Contents lists available at ScienceDirect

Results in Materials

journal homepage: www.sciencedirect.com/journal/results-in-materials

Effect of heat treatment on the microstructure characteristics and microhardness of a novel γ′ nickel-based superalloy by laser powder bed fusion

Jinghao Xu [a,*], Fiona Schulz [b], Ru Lin Peng [a], Eduard Hryha [b], Johan Moverare [a]

[a] Division of Engineering Materials, Department of Management and Engineering, Linköping University, Linköping, SE-58183, Sweden
[b] Division of Materials and Manufacture, Department of Industrial and Materials Science, Chalmers University of Technology, Gothenburg, SE-41296, Sweden

ARTICLE INFO

Keywords:
Nickel-based superalloy
LPBF
Heat treatment
Gamma prime γ′
Recrystallization

ABSTRACT

The fabrication of gamma prime (γ′) strengthened nickel-based superalloys by additive manufacturing (AM) techniques is of huge interest from the industrial and research community owing to their excellent high-temperature properties. The effect of post-AM-processing heat treatment on the microstructural characteristics and microhardness response of a laser powder bed fused (LPBF) γ′ strengthened nickel-based superalloy, MAD542, is systematically investigated. Post-processing heat treatment shows the significant importance of tailoring the γ′ morphology. With insufficient solutioning duration time, coarse γ′ formed in the interdendritic region heterogeneously, due to the lack of chemical composition homogenization. The cooling rate from the super-solvus solutioning plays an important role in controlling the γ′ size and morphology. Spherical γ′ is formed during the air cooling while irregularly shaped γ′ formed during the furnace cooling. The following aging heat treatment further tunes the γ′ morphology and γ channel width. After two-step aging, cuboidal γ′ is developed in the air-cooled sample, while in contrast, bi-modally distributed γ′ is developed in the furnace cooled sample with fine spherical γ′ embedded in the wide γ channel between coarse irregular shaped secondary γ′. More than 90% of the grains recrystallized during solutioning treatment at the super-solvus temperature for 30 min. The rapid recrystallization kinetics are attributed to the formation of annealing twins which significantly reduced the stored energy. Microhardness responses from different heat-treated conditions were examined.

1. Introduction

In recent years, the rapid development of metallic additive manufacturing (AM) techniques, e.g., laser powder bed fusion (LPBF), offers great potential for fabricating complex components of nickel-based superalloys for high-temperature applications. While a strong research focus has so far been on 'weldable' superalloys such as solid-solution strengthened superalloy Hastelloy X [4], and gamma double prime (γ″) strengthened superalloys IN625 [5] and IN718 [6], (gamma prime) γ′ strengthened superalloys are gaining increasing interest for LPBF processing due to their exceptional properties and high-temperature, high-performance applications. One of the biggest challenges regarding the implementation of the LPBF process on the γ′ strengthened superalloys is their high cracking susceptibility during LPBF. One approach described in recent research is to develop new γ′ strengthened superalloys by re-combining the chemical compositions, which then results in crack-free, as-fabricated material. For instance, by modifying the minor elements as well as with the assistance of printing parameter optimization, the legacy γ′ strengthened superalloys, such as IN738LC [7,8] and CM247LC (Hf-free derivative) [9], were reported to be fabricated in the crack-free or near crack-free conditions by LPBF process. Recently, via various alloy design approaches, newly developed superalloys, such as the MAD542 superalloy [10,11] with higher than 60 vol% γ′ fraction, ExpAM and ExpAM-mod superalloys [12] with 55 vol% γ′ fraction, and ABD-850/900AM [13] with low-to-moderate amounts of γ′, were additively manufactured by LPBF in the crack-free condition.

Both γ′ precipitation and the grain structure have a significant influence on the mechanical properties like strength, creep resistance, and fatigue performance, at the elevated temperature [14,15]. Heat treatment procedures for nickel-based superalloys are applied to achieve chemical homogenization and to control the grain structure.

* Corresponding author.
E-mail address: jinghao.xu@liu.se (J. Xu).

https://doi.org/10.1016/j.rinma.2021.100232
Received 23 August 2021; Received in revised form 26 September 2021; Accepted 8 October 2021
Available online 9 October 2021

Temperatures above the γ′-solvus temperature generally serve to remove severe elemental segregation and undesired phase configuration (e.g., γ/γ′ eutectics in as-cast single crystal superalloys). However, these high temperatures also promote grain growth due to γ′ dissolution, effectively removing Zener pinning of the grain boundaries, leading to coarse grain structures [16]. Therefore, the specific grain size requirements dictate heat treatment considerations at sub- and super-γ′-solvus temperatures [17,18]. Well-designed and controlled heating rates are especially important during super-γ′-solvus treatments to avoid localized incipient melting [19]. The γ′ characteristics determined by their precipitation events are largely dependent on the cooling rates. Controlled cooling combined with appropriate aging steps can achieve various γ′ size distributions such as unimodal, bimodal or even trimodal [20,21].

Material fabricated by means of LPBF experiences a complex thermal history during the process itself based on powder melting, layer remelting, and intrinsic heat treatment with very fast heating and cooling rates [22]. The resulting microstructure is complex and crystallographic textured grain structures are commonly reported for LPBF nickel-based superalloy which are associated with the anisotropic mechanical behavior. In the as-built microstructure, a large number of defects such as dislocation cellular walls and subgrain boundaries, are remained [23,24]. As examined by Kuo et al. [25], the creep rupture life of LPBF fabricated IN718 superalloys are much shorter than the cast and wrought counterpart which is attributed to the subgrain boundaries prohibit mobile dislocation and result in stress concentration at the crack tips. Under these bases, to serve at the elevated temperature, the well-recrystallized microstructure is of interest. However, sluggish recrystallization response of LPBF nickel-based superalloys is reported. For instance, reported by Kunze et al. [26], by hot isostatic pressed at super-γ′-solvus temperature for 4 h then following with a standard heat treatment, the recrystallized grain could still not be promoted in an LPBF IN738 superalloy. It indicates the recrystallization process which involves grain boundary migration by sweeping the stored energy gradient area is difficult.

Extensive work has been done for the conventionally processed γ′ superalloys, however, what is not yet well understood is the microstructural evolution of γ′ strengthened nickel-based superalloy by the LPBF process. In this study, an LPBF processed γ′ strengthened nickel-based superalloy was subjected to post-processing heat treatment conditions with different variants of solution treatment time, cooling method from solution treatment temperature, aging temperature, and aging duration time. The γ′ characteristics and grain structure with special focus on the recrystallization behavior correspond to different heat treatment conditions were systematically characterized and discussed.

2. Experimental procedures

2.1. Materials and manufacturing

The material investigated in this study was a γ′ strengthened nickel-based superalloy MAD542 with its nominal chemical composition listed in Table 1. The gas-atomized powder was supplied by Höganäs AB, Sweden with a particle size between 15 and 45 μm. The powder was consolidated in protective argon atmosphere using an EOS M100 LPBF system equipped with an ytterbium fiber laser with a full capacity of 200 W and an estimated laser spot size of 40 μm. To achieve the high metallurgical quality samples with minimum defects level, an optimized processing parameter was used as documented in Ref. [11].

2.2. Post-processing heat treatments

Coupon samples of 5 × 5 × 5 mm^3 were cut off from the as-built samples and then subjected to multi-variant heat treatment experiments. First, the thermal characteristics of the as-built MAD542 superalloy were determined using Differential Scanning Calorimetry (DSC) analysis with the results shown in Fig. 1. The DSC measurements were carried out on a NETZSCH STA449C thermo-microbalance system under the argon atmosphere with the argon flow of 50 ml/min. The DSC sample was firstly heated from room temperature to 600 °C with a heating rate of 20 °C/min, then the sample was hold and stabilized at 600 °C for 60 min. After then, the sample was heated up from 600 to 1400 °C at a heating rate of 10 °C/min, and maintained at 1400 °C for 10 min. The sample was then cooled from 1400 to 600 °C using a cooling rate of 10 °C/min. Two cycles were conducted for the same sample. Fig. 1 shows the curve from the first heating and cooling cycle.

Solution heat treatment steps are commonly applied to promote recrystallization of the microstructure. Based on the DSC finding, the solution heat treatment temperature is set to above the γ′ solvus with 1230 °C. In order to investigate the influence of dwell time, solution treatments were firstly carried out at 1230 °C for 10, 30, 60, and 120 min, followed by air-cooling. According to the results, a 2 h hold time at 1230 °C was determined for the solution heat treatment (detailed in Figs. 5 and 8). After the solution treatment, two different cooling approaches were used: air cooling (AC) and furnace cooling (FC). By attaching a K-type thermocouple to the sample surface, the cooling rates for AC and FC were found to be approximately 300 °C/min and 5–15 °C/min, respectively. Following the solution treatment, two different aging treatments were carried out either separately or as consecutive steps. The first aging temperature was set at 1080 °C, applied for 4 h, the second aging temperature was set at 900 °C and applied for 24 h, both followed by AC. The full list of heat treatment conditions and the denotations of samples are provided in Table 2. All the heat treatments were performed in a laboratory chamber furnace with an internal chamber dimension of 250 × 350 × 200 mm. The samples were put into the furnace after the target temperature was stabilized for at least 2 h. All the heat treatments were conducted in lab air.

2.3. Microstructural characterization and microhardness measurements

For microstructural characterization, metallographic samples were prepared by grinding and polishing to colloidal silica finish with a Struers OP-U suspension. Scanning electron microscopy (SEM) imaging was carried on a Hitachi SU70 SEM system coupled with energy-dispersive x-ray spectroscopy (EDS) and electron backscatter diffraction (EBSD). EBSD measurements were collected using the Oxford EBSD system (NORDLYS detector) at an acceleration voltage of 20 kV on well-polished samples. The cellular structure in the as-built condition was characterized by a FEI Tecnai G2 scanning transmission electron microscopy (STEM) operating at 200 kV accelerating voltage. STEM sample was prepared using twin-jet electropolishing on a Struers apparatus. The electropolishing was conducted at −25 °C in the 10% perchloric acid and 90% ethanol electrolyte solution. To reveal the morphology of γ′ precipitates, chemical etching and electro-etching methods were used. For chemical etching, the polished samples were immersed in Marble's reagent for 5–15 s at the ambient temperature, which dissolves the γ′ phase. For electro-etching, the well-polished samples were connected to the anode with a voltage of 10 V while a nickel plate was used as the cathode. The sample was immersed in the electrolyte of 10% phosphoric

Table 1
The chemical composition of the MAD542 nickel-based superalloy in this study.

Alloy	Cr	Co	Mo	W	Al	Ti	Ta	Nb	C	B	Si	Zr	Ni
MAD542 (wt.%)	8.0	8.0	5.0	4.0	5.0	1.0	3.0	2.0	0.1	<0.001	<0.005	<0.002	Bal.
MAD542 (at.%)	9.0	8.0	3.1	1.3	10.9	1.2	1.0	1.3	0.5	<0.005	<0.01	<0.001	Bal.

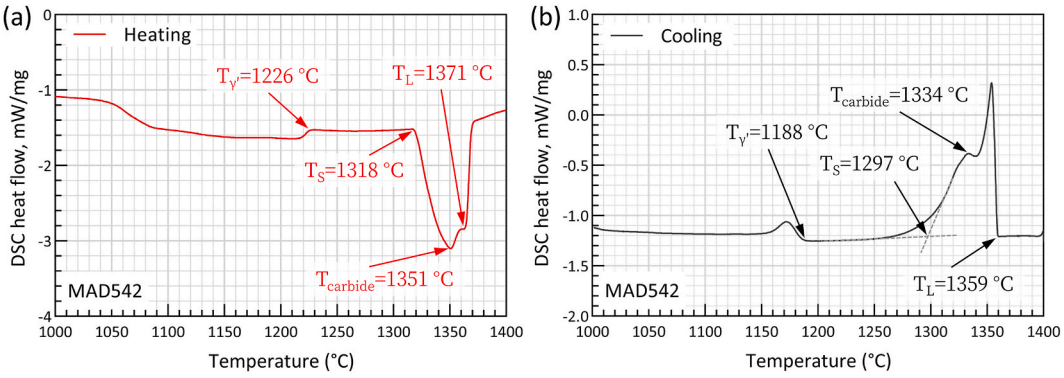

Fig. 1. DSC analysis on the as-built MAD542 superalloy determining the γ′ solvus ($T_{\gamma'}$), solidus (T_S), carbide dissolution ($T_{carbide}$), and liquidus temperature (T_L) for the respective (a) heating, and (b) cooling curve.

Table 2
Heat treatment conditions used in this study.

Sample	Temp. of solutioning (2 h), °C	Cooling from solutioning temp.	Temp. of first aging (4 h), °C	Temp. of second aging (24 h), °C
AB (as-built)	–	–	–	–
AC	1230	AC	–	–
AC-age1	1230	AC	1080	–
AC-age1-age2	1230	AC	1080	900
AC-age2	1230	AC	–	900
FC	1230	FC	–	–
FC-age1	1230	FC	1080	–
FC-age1-age2	1230	FC	1080	900
FC-age2	1230	FC	–	900

acid solution, and the electro-etching time lasted for approximately 5 s for each sample, dissolving the γ matrix while γ′ precipitates remain.

Vickers microhardness tests were performed on the polished samples using a Struers DuraScan G5 hardness test system. A 3 × 3 indentation matrix was carried out for each sample with a 300-g load (HV0.3) which resulted in indents with a diagonal length between 30 and 40 μm. The interspacing between nearest indents was 400 μm, which was 10 times larger than the size of each individual indent. To minimize the influence of anisotropic mechanical properties of the LPBF sample, all the indentations were carried on the planes normal to the LPBF building direction.

3. Results and discussions

3.1. As-built microstructure

Fig. 2 shows the as-built microstructure of the LPBF MAD542 superalloy. After chemical etching, the melt pool microstructure, as well as the grain boundaries, are revealed. The width of the melt pools is approximately 40–80 μm, which corresponds to the laser beam diameter. In this study, the melt pool width is 2–4 times greater than the powder layer thickness of 20 μm, which is the key to ensure the connection and continuity between layers. From the contrast of the etched sample, the grain boundaries can be observed, as indicated in Fig. 2(a). Elongated grains with columnar morphology are shown in the as-built microstructure. The direction of the longer length of these columnar grains is consistent with the building direction. It should be noted that the columnar grain boundary is not necessarily blocked by the melt pool boundary, as clearly shown in Fig. 2(b). Governed by the heat dissipation direction, the growth direction of the solidification dendrite is generally parallel to the normal direction of the melt pool boundary.

Microstructural features including cellular structures, elemental distribution, and dislocations structures of the as-built MAD542 sample are illustrated in Fig. 3. From the overview of Fig. 3(a), the cellular structures are observed in a broad dimensional range, indicating it is the unit of solidification structure. The general morphology of the cellular structures is shown by SEM (backscattered electron) BSE imaging at different magnifications (Fig. 3(a–c)). The intercellular spacing is less than 500 nm (Fig. 3(c)). However, depending on the orientation of the different grains, the morphology of the cellular structures varies (Fig. 3 (b)).

The cellular structure in as-built LPBF superalloys appears in two ways: the solidification dendrite and the deformation cells as shown in

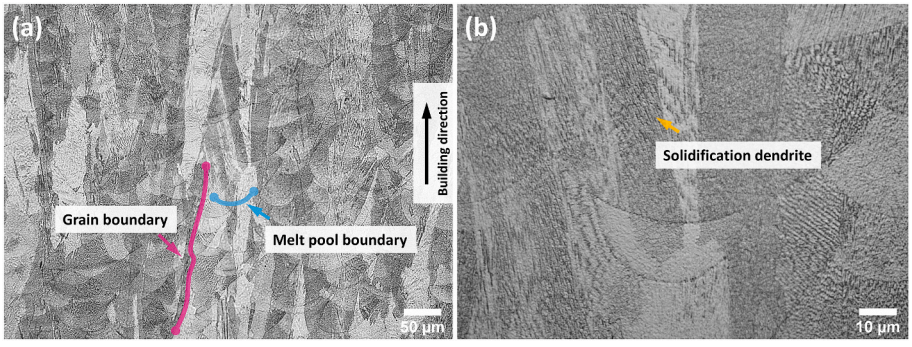

Fig. 2. Optical micrograph of the as-built MAD542 superalloy in the chemical etched condition, (a) overall view of the columnar grains as well as the melt pool, (b) enlarged view revealing the solidification dendrite.

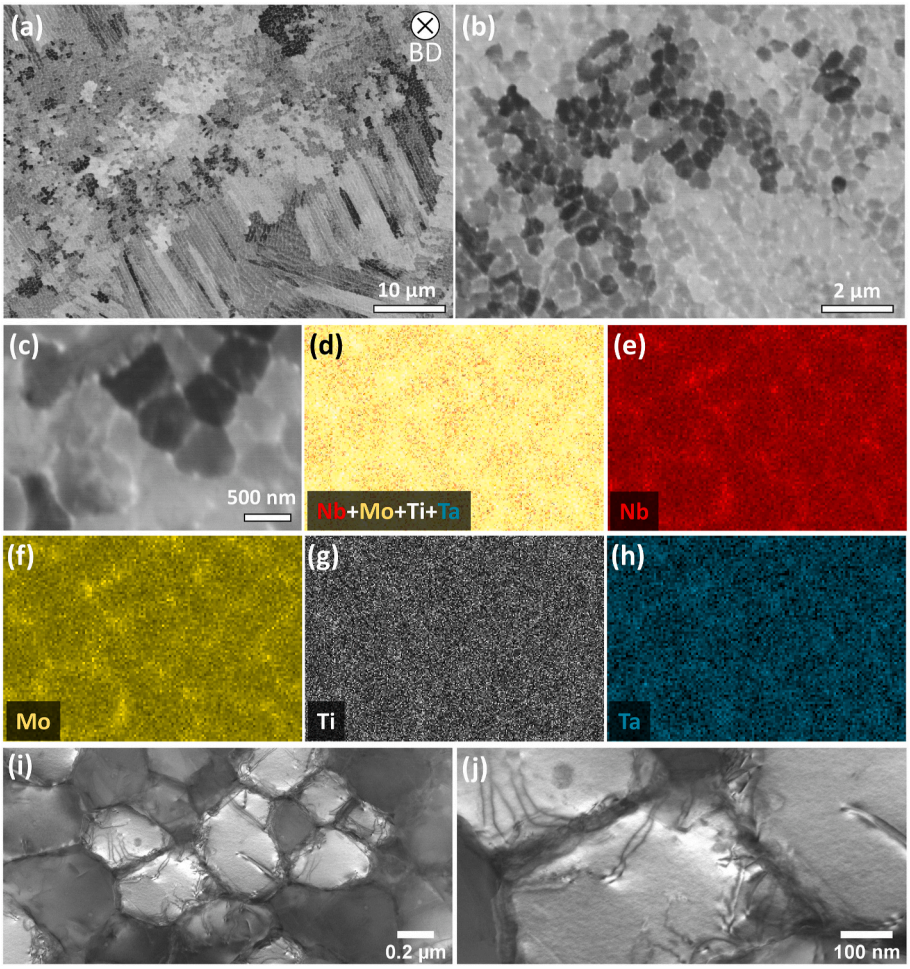

Fig. 3. (a–c) BSE SEM micrographs of the cellular structures in the as-built condition, (d–h) EDS chemical composition distribution map of the region (c), (i–j) BF-STEM micrographs of cellular structure as well as the dislocations. The building direction (BD) is perpendicular to the screen plane.

Fig. 3(d–h) and 3(i-j), respectively. The chemical composition maps of the EDS results, demonstrate/show that certain elements are enriched in the cellular boundaries. As shown in Fig. 3(d–h), the elements segregating to the cellular boundaries which were likely pushed from the already solidified dendrite core to the interdendritic region during solidification. This microsegregation behavior is consistent with that observed in conventional casting [27–29] and directional solidification [30,31]. The segregation of Nb, Mo, Ti, and Ta towards cellular boundaries has also been reported for other AM superalloys [23,32–34]. Besides cells formed through microsegregation, deformation cells could be observed via bright-field (BF) STEM micrographs (Fig. 3(i and j)). The dimension scale of the cellular structure is identical for both the SEM and STEM imaging. The STEM micrographs show the cellular boundaries as darker region. This region comprises a greater number of defects which can be identified as a high density of dislocations at higher magnification (Fig. 3(j)).

Due to the thermal dissipation heterogeneities during LPBF processing, small misorientations between the cells/within the cellular structure are developed. EBSD fine scanning of the as-built MAD542 superalloy with a scanning step size of 40 nm, equivalent to 1/10 of the average size of cellular interspacing size is presented in Fig. 4. Fig. 4(a) shows the band contrast (BC) map from EBSD measurement. The white pixels indicate the unindexed areas that are mainly on the high angle grain boundaries. Reflected by the Kikuchi pattern quality, the cellular boundary regions are illustrated darker as the black arrows indicate. To present the localized intragranular misorientations, the Kernel average misorientation (KAM) coloring map is shown in Fig. 4(b). The high-angle grain boundaries with a great than 10° misorientation angle

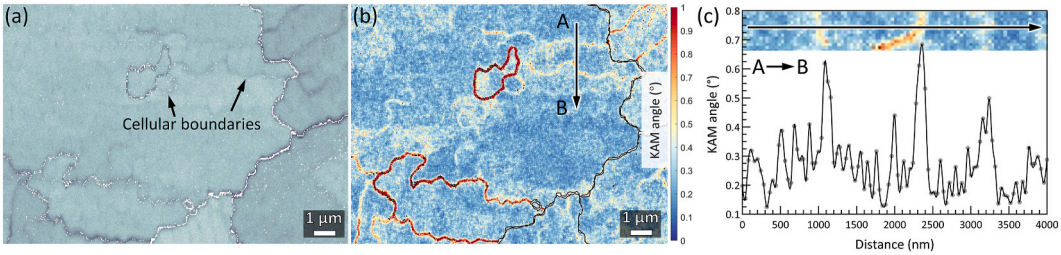

Fig. 4. (a) EBSD BC map of the as-built MAD542 superalloy, (b) KAM coloring map from the EBSD scanning area of (a), the color bar is shown on the right-hand side, (c) plot of KAM angle distribution profile as a function of distance along the point A to B marked in (b).

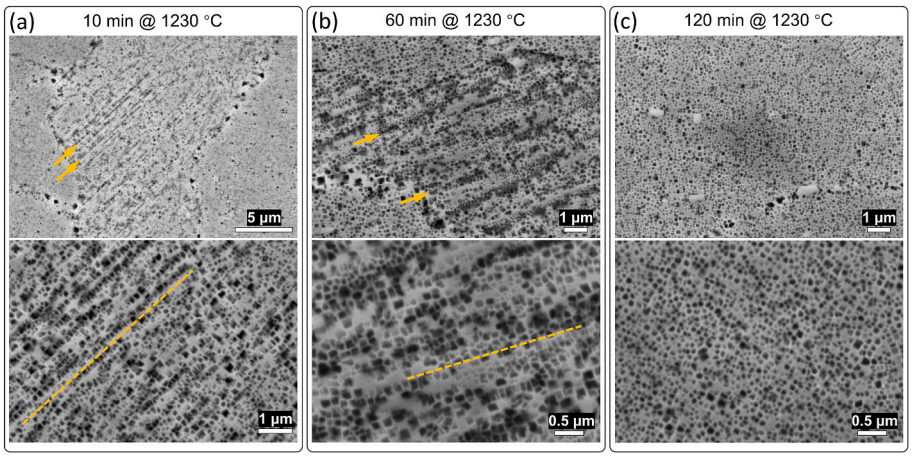

Fig. 5. Secondary electron SEM imaging of the chemical etched samples revealing the γ′ precipitates of (a) solutioning heat-treated at 1230 °C for 10 min, (b) 1230 °C for 60 min, and (c) 1230 °C for 120 min. All the specimens were air-cooled.

were excluded on calculating of KAM angle. The color scale in the range of 0–1° was added to visualize the small misorientations. Those boundaries with the misorientation angle between 1 and 10° were colored in red, which is the maximum coloring value. And these boundaries are considered as low-angle grain boundaries. In the as-LPBF-processed superalloys, the grain boundaries for both high- and low-angle ones, are overlapping with the cellular boundaries [10], since most of these grain boundaries are solidification grain boundaries, which formed at the last stage of the solidification process. Of special interest here is the cellular boundaries with small misorientation angles below 1°. As shown in Fig. 4(b), these cellular boundaries generally have a relatively higher value of KAM angle compared with the cellular interior regions. Based on the qualitative estimation from the color bar (Fig. 4(b)), these cellular boundaries typically have the larger KAM angles greater than 0.4°. The line profile measurement of the KAM distribution as a function of distance was conducted from point A to B in Fig. 4(b), and it is summarized and plotted in Fig. 4(c). The peak position of KAM angles is consistent with the position of cellular boundaries. To compensate for these misorientations, geometrically necessary dislocations were developed in the cellular boundary regions. It has been reported in the LPBF processed 316 L stainless steel [35,36], nickel-based superalloy [23,37], as well as pure copper [38].

3.2. The variation of γ′

Fig. 5 shows the SEM micrographs of chemically etched samples after heat treatment at 1230 °C for different times: 10 min, 60 min and 120 min. For all three conditions, γ′ precipitates were observed which formed during the cooling process from the super-γ′-solvus temperature. With shorter duration time at the solutioning temperature, coarser γ′, aligned with the interdendritic region, is observed (indicated by the dash-lines). The interdendritic region is enriched with the γ′ formers like Al and Ti because of the segregation during solidification. This finding is similar to the observation that coarser γ′ exists at the interdendritic region in the cast superalloy [39].

The solution heat treatment of the nickel-based superalloys with high content of refractory elements has been considered as a challenging step. Due to the low diffusivities of these elements as well as the long diffusion path from dendrite core to interdendritic region, these superalloys are difficult to be heat treated into the chemical homogenization. On the other hand, owing to the remaining γ/γ′ eutectic phase left behind in the interdendritic region during the solidification process, the local solidus temperature is lower than the solidus temperature of the alloy. If the solutioning temperature is set imprudently, incipient melting will occur. To this sense, the solutioning of these superalloys by conventional processing requires a long time. Well-designed heating scenarios will be needed to mitigate the risk of incipient melting and achieve chemical homogenization for certain superalloys [19].

For additively manufactured superalloys, the fine dendrite arm spacing undoubtedly benefits the reducing of solutioning time. In additively manufactured nickel-based superalloys, compared with conventionally cast or directionally solidified alloys, much finer primary dendrite arm spacing (PDAS) is observed in the as-built condition. Specifically, in a single crystal superalloy fabricated by directional solidification, the PDAS varies from tens to hundreds of micrometers depending on the combination of thermal gradient and growth rate [40]. However, in the LPBF superalloy, the primary dendrite arm spacing is equivalent to the interspacing of the cellular structure, i.e. on sub-micron level. As reported by Ramsperger et al. [41], the complete chemical homogenization could be reached in 4 min at 1310 °C for the electron beam melted CMSX-4 superalloy. In contrast, the typical solutioning heat treatment requires multiple steps of heating from 1276 to 1324 °C with a total exposure time of 19 h excluding the heating time during ramping [42], for the same superalloy produced by directional solidification. Based on the observation in Fig. 5, for LPBF fabricated γ′ strengthened nickel-based superalloy, although the solutioning treatment duration time is supposed to be decreased, detailed γ′ characterization is necessary to confirm if the uniform γ′ precipitates developed.

During cooling from a temperature above the γ′ solvus temperature, the γ′ develops differently depending on the applied cooling rates. Fig. 6 shows the γ′ morphology and dimensional scale of the γ′ after different heat treatment conditions. In the as-solutionized sample (1230-AC and 1230-FC for air cooling and furnace cooling, respectively), the size of γ′ is directly associated with the cooling rates. In this study, the γ′ precipitate size is defined as the equivalent diameter of the precipitate area measured during image analysis. In the air-cooled sample (1230-AC), near-spherical γ′ is observed with the size of 71 nm on average (std. 13 nm). However, in the furnace-cooled sample (1230-FC), coarse γ′ was developed with a mean size of 823 nm as well as a less even size distribution with a standard deviation of 470 nm. In the literature regarding the effect of heat treatment on the γ′ precipitation, this phenomenon was reported for a powder-metallurgy disc superalloy [43].

During the isothermal heat treatment, i.e. aging at a constant temperature in this study, the coarsening of γ′ in the supersaturated matrix could be formulated by a time-dependent fashion according to the classical Lifshitz and Slyozov [44] and Wagner [45] (LSW) theory. It describes the difference of precipitate sizes (in volume dimension scale) after and before aging is governed by the coarsening coefficient and aging time. Based on theories, the size of γ′ apparently increased in the air-cooling samples after aging. In contrast, no obvious γ′ growth with regard to the precipitate size is observed in the furnace-cooling samples after aging. Instead, the morphology changes are observed. Slow cooling

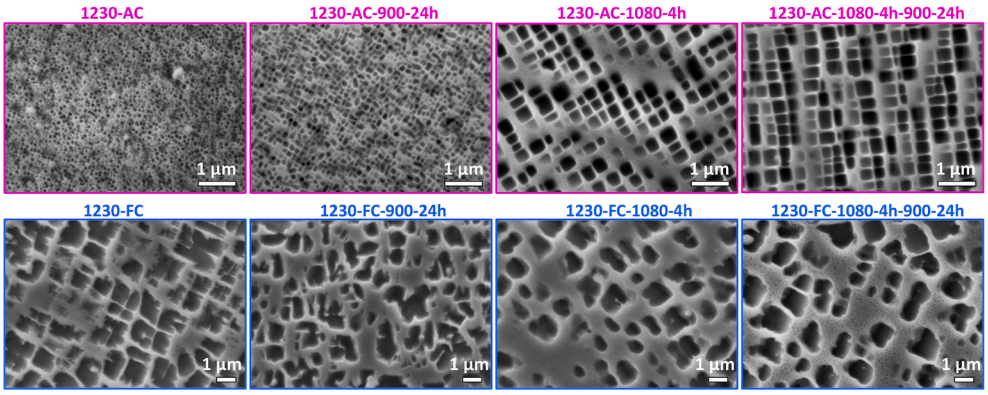

Fig. 6. SEM secondary electron imaging of the γ′ morphologies of different heat-treated samples.

rate, like furnace cooling in this study, leads to the extended growth of γ′ during cooling, which drives the supersaturation largely reduced in the matrix. After then, during isothermal aging steps, Ostwald ripening occurs caused by decreasing the total surface area of γ′ precipitates [46]. Consequently, it is evident that the γ′ with a sharp corner in the as-cooled sample turned into the γ′ with round corners in the aged samples.

The different γ channel widths of the first-aged air-cooling and furnace-cooling samples are one of the most distinct features. It then controls the γ′ distribution after two-step aging. Another interesting result is the different behavior with response to the two-step aging processes, as the SEM micrographs shown in Fig. 6. In the air-cooling samples, the cuboidal γ′ with round corners was developed at the first aging at 1080 °C for 4 h. Meanwhile, the γ channel width is 52 nm on average. The coarser γ′ was developed after aging at 900 °C for 24 h following the first aging (Fig. 7(a)). The diffusional growth of γ′ continues as evidence as to the γ channel width decrease from 52 nm to 42 nm. In the contrast, large γ channel width was observed in the first-aged furnace cooling sample, in the dimension scale of several hundreds of nanometers to several micrometers. After the two-step aging, another population of fine γ′ burst in between coarse γ′ (Fig. 7(b)). This fine γ′ is in a spherical shape with a fine size of 20–100 nm in diameter.

3.3. The variation of grain structure

One of the more important purposes of doing a super-solvus solutioning heat treatment of LPBF superalloys is to achieve a recrystallized grain structure. In this study, the recrystallization (RX) is measured by EBSD characterization, where the RX grains are defined as the grains which have a grain orientation spread (GOS) value less than 1°. To visualize this, the RX grains are plotted in the RX map with RX grains colored in blue. In the as-built condition, RX grains are barely found which is consistent with the high dislocation density within the as-built microstructure (Fig. 3). The evolution of recrystallized grains and twin

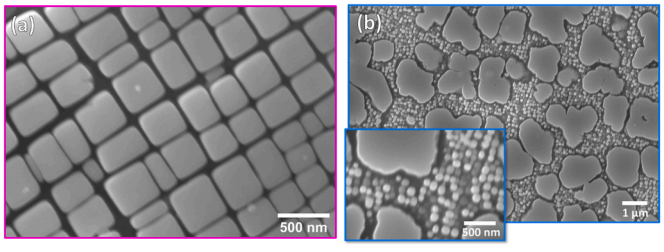

Fig. 7. SEM micrographs of electro-etched samples after solution heat treatment (1230 °C/2 h) with different cooling rates followed by a two-step aged treatment (1080 °C/4 h + 900 °C/24 h). (a) air cooling from solution treatment and (b) furnace cooling from solution treatment.

boundaries as a functional form of hold time is shown in Fig. 8. A quick recrystallization response could be identified for the LPBF MAD542 superalloy annealed at 1230 °C. After solutioning heat treatment for 30 min, more than 90% area fraction of RX grains were developed. Typically, the grain structure evolution undergoes three stages: recovery, recrystallization, and grain growth. For nickel-based superalloys highly doped with alloying elements, the recovery process hardly takes place by the means of rearrangement and/or annihilation of dislocations [47,48]. Additionally, low stacking fault energy is generally obtained by nickel-based superalloys [49,50], which leads to the wide separation between partial dislocations. Therefore, dislocation climb and cross-slip are difficult to realize, which are the basic approaches for recovery. Then, the recrystallization process is instead associated with the grain boundary migration. In fact, sluggish RX behaviors of LPBF γ′ strengthened nickel-based superalloys have been reported [26,51–53]. For instance, Zener pinning effects from grain boundary precipitates provides a significant pressure against the grain boundary migration in the comparable scale of driving pressure derived from stored energy [54].

As shown in the RX map in Fig. 8, the MAD542 superalloy shows a good recrystallization response. First, it is owing to the solutioning heat treatment at super-solvus temperature, which reduced the effect of Zener pinning by the dissolution of grain boundary γ′ precipitates. However, it should be pointed out, that the RX happens with the assistance of twin boundary (TB) formation, as summarized in the plot of TB evolution as a function of holding time at 1230 °C. Accomplished with greater than 90% of RX grains after 30 min, more than 55% (in length percentage) of TBs are retained.

In Fig. 9, a pair of parent and twin grains are selected from the EBSD results of a sample from solutioning treatment at 1230 °C for 2 h. The building direction is horizontally parallel to the X-direction of the EBSD scan (indicated in Fig. 9(b)). Fig. 9(a) shows the inverse pole figure (IPF) coloring map of the parent and twin grains. The grain colored in red is likely to be the parent grain due to the [001] direction which is primarily aligned with the building direction (EBSD X-direction), while the twin is colored in blue. The (111) pole figure of the upper hemisphere stereographic projection is shown in Fig. 9(b). The interface of the twin boundary shown in Fig. 9(a) is in good agreement with the trace of the shared (111) planes. In addition, the misorientation angle could be calculated from the Euler angles from the mean grain orientation of parent (223°, 172°, 221°) and twin (293°, 129°, 234°). In this case, the minimum value of misorientation is determined to be 59.9989°. The crystallographic orientation of the twin is more uniform as indicated by the highly concentrated spots in the pole figure. In contrast, the parent grain is more misoriented compared to the twin. The promoted twin shows a highly recrystallized structure, with the GOS value of 0.1892°, as well as the parent grain which shows a GOS value of 0.2916°. It indicates that recrystallized grains are effectively introduced by the formation of twin boundaries, as widely reported from the literature [55,

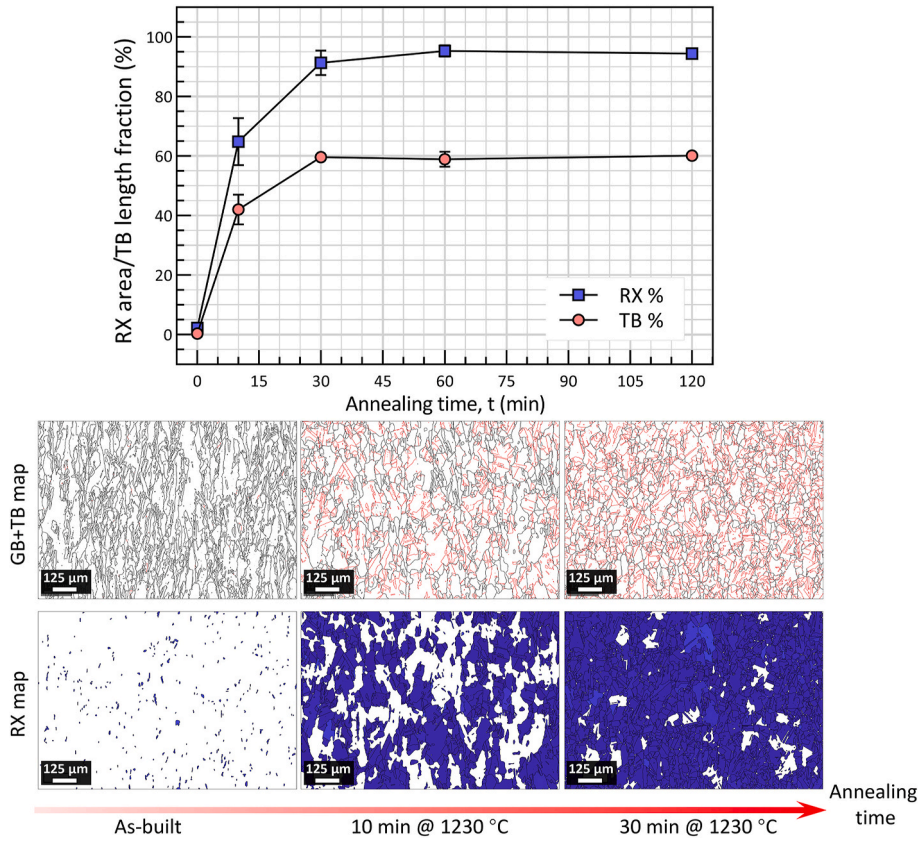

Fig. 8. The twin boundary (TB) and recrystallization (RX) fraction evolution as a function of annealing time at 1230 °C, indicating a combination of rapid RX and TB formation processes. The EBSD scans cover an area of 870 µm × 1266 µm with a 2-µm step size. In the GB + TB maps, the grain boundaries (GB) are plotted in black lines, while TBs are plotted in red lines. In the RX maps, RXed grains are colored in blue. Error bars correspond to the standard deviation.

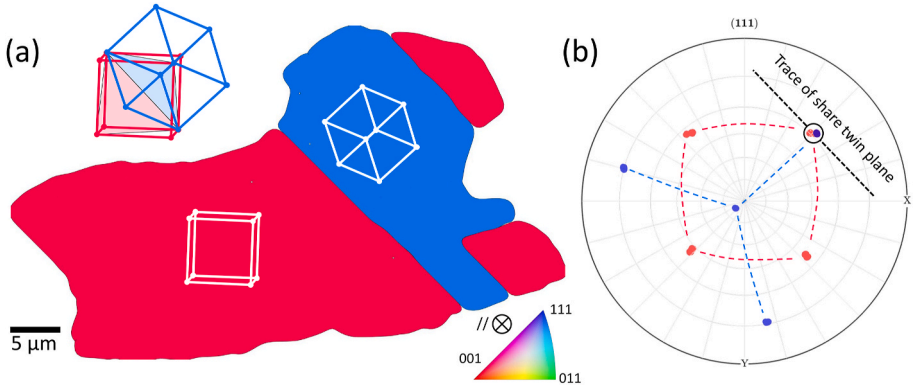

Fig. 9. (a) IPF coloring map of the parent and twin grain of a 1230 °C solutioning treated MAD542 sample and (b) (111) pole figure of the corresponding grains.

56]. It is not surprising that the large fraction TB boundaries formed in LPBF MAD542 superalloy since the low stacking fault energy leads to the high susceptibility of the formation of annealing twins [57]. The stacking fault energy heavily relies on the chemical composition and for the MAD542 superalloy, the relatively higher concentration of Mo and Nb (comparing with other cast heritage superalloys like IN738LC, IN939, and CM247LC) is one of the most significant features in the composition perspective. The Mo and Nb are the two most effective stacking fault energy reducers among the common alloying elements in the Re-free nickel-based superalloys [49]. The extensive formation of TBs also mitigates the risk of internal post-processing cracking during heat treatment and is discussed in Ref. [11].

The distribution profiles of the grain boundary misorientation angle for different heat-treated MAD542 samples are illustrated in Fig. 10. It should be noted that the number fraction in percentage is used for Y-axis on a logarithmic scale. In the as-built sample, a large proportion of low angle grain boundary, which has the misorientation typically in 2–10°, is observed. These low-angle grain boundaries are correlated with the misorientation angles introduced by the dislocation networks on the cellular boundaries (Fig. 4). In the various heat treatment conditions, the primary peak of misorientation angle could be found at 60°, which is identified by the large proportion of annealing twin boundaries. By comparing the heat-treated sample with the as-built sample, the low angle grain boundaries were largely reduced, which is therefore consistent with the high degree of recrystallization after solutioning treatment (Figs. 8–9). For all the heat-treated samples, the distribution

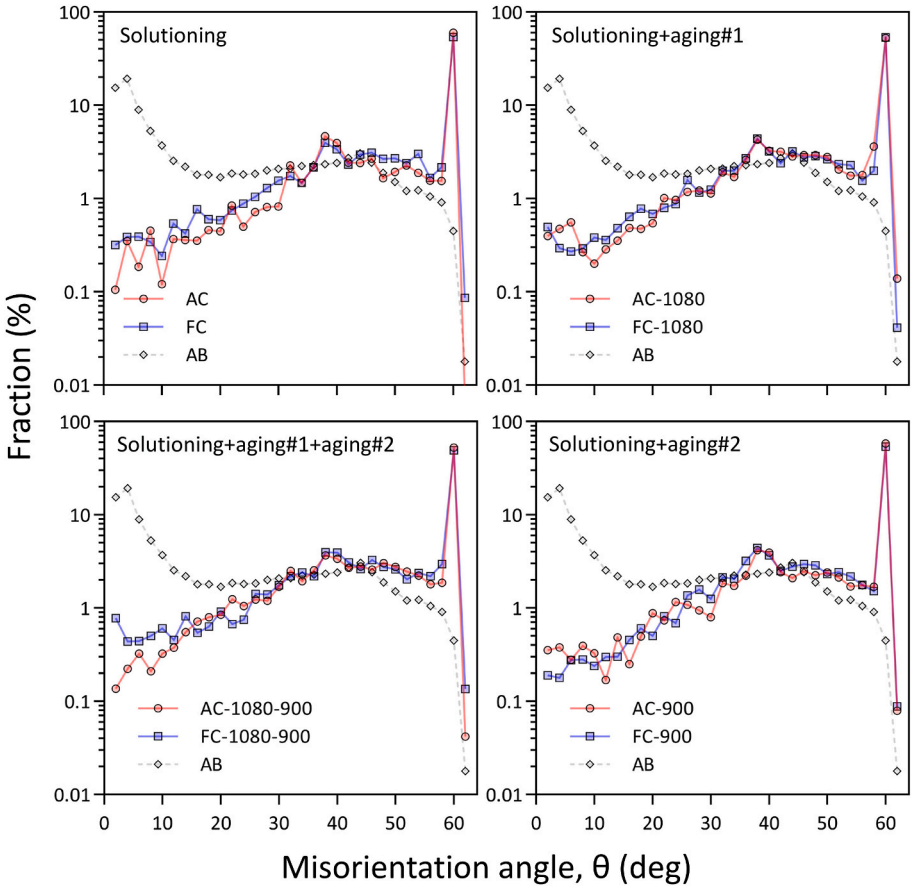

Fig. 10. Grain boundary misorientation angle distribution of the different heat-treated MAD542 comparing with the as-built microstructure.

profiles of misorientation angles are generally consistent. It indicates the grain boundary misorientation is less sensitive to the cooling rate from solutioning treatment, aging temperature, aging time, but governed by the solutioning step, which is 1230 °C for 2 h for all the samples.

3.4. Microhardness

Fig. 11 summarizes the Vickers microhardness (HV0.3) test results of all heat treatment variants considered in this study. The error bars indicate the standard deviation, while the HV0.3 values for as-built specimen are plotted in the grey band. The corresponding

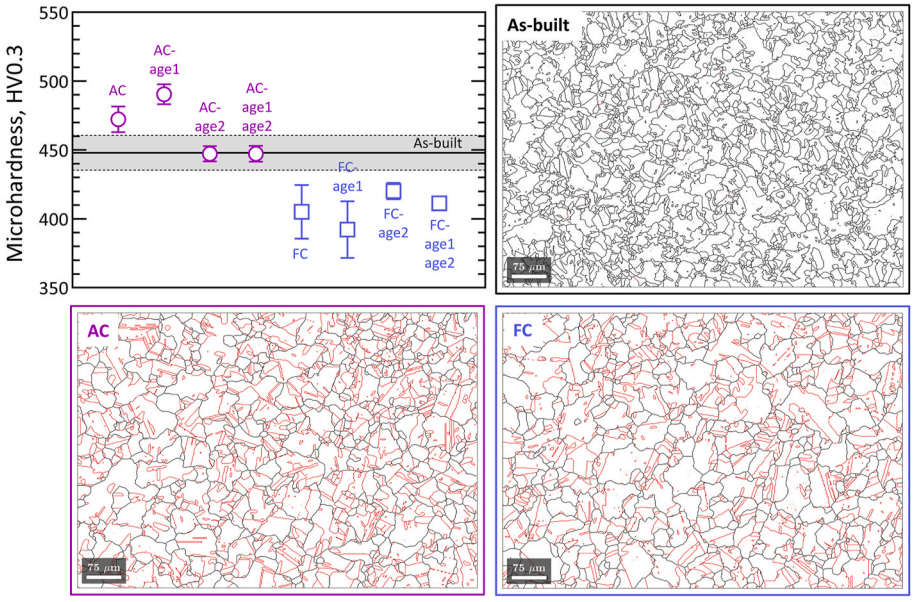

Fig. 11. Microhardness results of LPBF MAD542 superalloy under different treatments with the corresponding EBSD grain boundary (in black) and twin boundary plots of representative conditions.

microstructures of as-built, AC, and FC samples are presented in terms of grain boundary and twin boundary plots. According to the characterizations shown in previous sections (Figs. 3 and 6), γ′ precipitates were developed after heat treatment while barely any γ′ was observed in the as-built sample. However, the hardness value (448 HV0.3 on average) of the as-built sample is comparable to the γ′ containing samples. Despite the absence of precipitation hardening of γ′, the as-built sample is therefore highly strengthened by the high-density dislocation walls (Fig. 3). It has been considered as the unique benefit on the room-temperature mechanical properties of LPBF processed metallic materials like 316 L stainless steels [36], and high entropy alloys [58]. The hardness differences among the heat-treated samples, where no significant deviation of grain sizes is obtained, are principally affected by the precipitation hardening effect of γ′. Among the heat-treated samples, the hardness shows a general dependence on the size of γ′. The large values of microhardness were observed in the samples from 1230-AC and 1230-AC with aging at 900 °C for 24 h, owing to the fine γ′ sizes (Fig. 6). In contrast, the samples consisting of coarse γ′ from furnace cooling generally show lower values of hardness. The size of γ′ largely affects the precipitate and dislocation interaction, for example, dislocation shearing of fine precipitates and Orowan looping of coarse precipitates [59]. Moreover, the strengthening effects on the LPBF γ′ strengthened nickel-based superalloy in relation to the as-built microstructure are discussed in detail in the previous publication [37].

4. Conclusions

In this study, the effects of post-processing heat treatment on the γ′ characteristics, recrystallization, grain structure, and microhardness of a laser powder bed fused γ′ strengthened nickel-based superalloy was investigated. Owing to the inherent high cooling rate of the LPBF process, the solidification dendrite structure is several orders finer than the conventionally processed counterparts. It helps to reduce the duration time of solutioning heat treatment. However, insufficient solutioning time led to the heterogeneous size distribution of γ′ in the grain interior. In the interdendritic region, coarse γ′ existed with short solutioning time. The γ′ morphology is sensitive to the cooling rates from the supersolvus temperature. Fine spherical γ′ with 71 nm in diameter was formed by air cooling, while coarse irregular shaped γ′ with a size of 823 nm formed by furnace cooling. After a two-step aging, unimodal cuboidal γ′ were formed in the air-cooled sample while bimodal γ′ developed in the furnace cooled sample, which is associated with the diffusion-controlled γ′ growth in the isothermal conditions. By promoting the extensive twin boundaries, it allows the rapid recrystallization of LPBF γ′ strengthened nickel-based superalloy at the super-γ′-solvus temperature. The grain size and grain boundary microrotation is dominated by the solutioning temperature and shows less dependency on the cooling method and the isothermal aging steps. The microhardness of the heat-treated samples is controlled by the precipitation strengthening mechanism.

CRediT author statement

Jinghao Xu: Conceptualization, Methodology, Validation, Formal analysis, Investigation, Data Curation, Writing - Original Draft, Writing - Review & Editing, Visualization. **Fiona Schulz**: Methodology, Validation, Investigation, Data Curation, Writing - Review & Editing. **Ru Lin Peng**: Methodology, Investigation, Writing - Review & Editing, Supervision. **Eduard Hryha**: Resources, Writing - Review & Editing, Funding acquisition. **Johan Moverare**: Conceptualization, Resources, Writing - Review & Editing, Supervision, Project administration, Funding acquisition.

Declaration of competing interest

The authors declare that they have no known competing financial interests or personal relationships that could have appeared to influence the work reported in this paper.

Acknowledgments

This work was supported by the Swedish Agency for Innovation Systems, (Vinnova grant 2016-05175 and 2018-00804); faculty grant from Linköping University (SFO-MAT-LiU#2009-00971); and center for Additive Manufacture – Metal (CAM^2). J.X. is grateful to Dr. H. Gruber for LPBF assistance.

All data included in this study are available from the corresponding author on reasonable request.

References

[4] C.-H. Yu, R.L. Peng, V. Luzin, M. Sprengel, M. Calmunger, J.-E. Lundgren, H. Brodin, A. Kromm, J. Moverare, Thin-wall effects and anisotropic deformation mechanisms of an additively manufactured Ni-based superalloy, Addit. Manuf. (2020) 101672, https://doi.org/10.1016/j.addma.2020.101672.

[5] F. Zhang, L.E. Levine, A.J. Allen, M.R. Stoudt, G. Lindwall, E.A. Lass, M. E. Williams, Y. Idell, C.E. Campbell, Effect of heat treatment on the microstructural evolution of a nickel-based superalloy additive-manufactured by laser powder bed fusion, Acta Mater. 152 (2018) 200–214, https://doi.org/10.1016/j.actamat.2018.03.017.

[6] D. Deng, R.L. Peng, H. Brodin, J. Moverare, Microstructure and mechanical properties of Inconel 718 produced by selective laser melting: sample orientation dependence and effects of post heat treatments, Mater. Sci. Eng. A. 713 (2018) 294–306, https://doi.org/10.1016/j.msea.2017.12.043.

[7] M. Cloots, K. Kunze, P.J. Uggowitzer, K. Wegener, Microstructural characteristics of the nickel-based alloy IN738LC and the cobalt-based alloy Mar-M509 produced by selective laser melting, Mater. Sci. Eng. A. 658 (2016) 68–76, https://doi.org/10.1016/j.msea.2016.01.058.

[8] N. Perevoshchikova, J. Rigaud, Y. Sha, M. Heilmaier, B. Finnin, E. Labelle, X. Wu, Optimisation of selective laser melting parameters for the Ni-based superalloy IN-738 LC using Doehlert's design, Rapid Prototyp. J. 23 (2017) 881–892, https://doi.org/10.1108/RPJ-04-2016-0063.

[9] S. Griffiths, H. Ghasemi Tabasi, T. Ivas, X. Maeder, A. De Luca, K. Zweiacker, R. Wróbel, J. Jhabvala, R.E. Logé, C. Leinenbach, Combining alloy and process modification for micro-crack mitigation in an additively manufactured Ni-base superalloy, Addit. Manuf. 36 (2020) 101443, https://doi.org/10.1016/j.addma.2020.101443.

[10] J. Xu, Alloy Design and Characterization of γ′ Strengthened Nickel-Based Superalloys for Additive Manufacturing, Linköping University Electronic Press, 2021, https://doi.org/10.3384/lic.diva-173042.

[11] J. Xu, H. Gruber, R. Lin Peng, J. Moverare, A novel γ′-strengthened nickel-based superalloy for laser powder bed fusion, Materials 13 (2020) 4930, https://doi.org/10.3390/ma13214930.

[12] N. Zhou, A.D. Dicus, S.A.J. Forsik, T. Wang, G.A. Colombo, M.E. Epler, Development of a new alumina-forming crack-resistant high-γ′ fraction Ni-base superalloy for additive manufacturing, TMS Superalloys 2020 (2020) 1046–1054, https://doi.org/10.1007/978-3-030-51834-9_102.

[13] Y.T. Tang, C. Panwisawas, J.N. Ghoussoub, Y. Gong, J. Clark, A. Németh, D. G. McCartney, R.C. Reed, Alloys-by-design: application to new superalloys for additive manufacturing, Acta Mater. (2020), https://doi.org/10.1016/j.actamat.2020.09.023.

[14] R.W. Kozar, A. Suzuki, W.W. Milligan, J.J. Schirra, M.F. Savage, T.M. Pollock, Strengthening mechanisms in polycrystalline multimodal nickel-base superalloys, Metall. Mater. Trans. 40 (2009) 1588–1603, https://doi.org/10.1007/s11661-009-9858-5.

[15] D.M. Collins, H.J. Stone, A modelling approach to yield strength optimisation in a nickel-base superalloy, Int. J. Plast. 54 (2014) 96–112, https://doi.org/10.1016/j.ijplas.2013.08.009.

[16] J.E. Burke, D. Turnbull, Recrystallization and grain growth, Prog. Met. Phys. 3 (1952) 220–292, https://doi.org/10.1016/0502-8205(52)90009-9.

[17] J. Xu, Z. Huang, L. Jiang, Low cycle fatigue behavior of a high Co polycrystalline nickel-base superalloy at 750 °C, J. Alloys Compd. 749 (2018) 1106–1114, https://doi.org/10.1016/j.jallcom.2018.03.364.

[18] D.P. M, S.H.R. B, E.M. L, R.J. Schirra, Superalloy optimized for high-temperature performance in high-pressure turbine disks, U. S. Jpn. Outlook 6 (175 B1) (1998) 521.

[19] E.C. Caldwell, F.J. Fela, G.E. Fuchs, The segregation of elements in high-refractory-content single-crystal nickel-based superalloys, JOM 56 (2004) 44–48, https://doi.org/10.1007/s11837-004-0200-9.

[20] P.M. Sarosi, B. Wang, J.P. Simmons, Y. Wang, M.J. Mills, Formation of multimodal size distributions of γ′ in a nickel-base superalloy during interrupted continuous cooling, Scripta Mater. 57 (2007) 767–770, https://doi.org/10.1016/j.scriptamat.2007.06.014.

[21] F. Schulz, H.Y. Li, H. Kitaguchi, D. Child, S. Williams, P. Bowen, Influence of tertiary gamma prime (γ′) size evolution on dwell fatigue crack growth behavior in CG RR1000, Metall. Mater. Trans. 49 (2018) 3874–3884, https://doi.org/10.1007/s11661-018-4779-9.

[22] P. Kürnsteiner, M.B. Wilms, A. Weisheit, P. Barriobero-Vila, E.A. Jägle, D. Raabe, Massive nanoprecipitation in an Fe-19Ni- x Al maraging steel triggered by the

intrinsic heat treatment during laser metal deposition, Acta Mater. 129 (2017) 52–60, https://doi.org/10.1016/j.actamat.2017.02.069.
[23] V.D. Divya, R. Muñoz-Moreno, O.M.D.M. Messé, J.S. Barnard, S. Baker, T. Illston, H.J. Stone, Microstructure of selective laser melted CM247LC nickel-based superalloy and its evolution through heat treatment, Mater. Char. 114 (2016) 62–74, https://doi.org/10.1016/j.matchar.2016.02.004.
[24] H. Hyer, R. Newell, D. Matejczyk, S. Hsie, M. Anthony, L. Zhou, C. Kammerer, Y. Sohn, Microstructural development in as built and heat treated IN625 component additively manufactured by laser powder bed fusion, J. Phase Equilibria Diffus. 42 (2021) 14–27, https://doi.org/10.1007/s11669-020-00855-9.
[25] Y.L. Kuo, S. Horikawa, K. Kakehi, Effects of build direction and heat treatment on creep properties of Ni-base superalloy built up by additive manufacturing, Scripta Mater. 129 (2017) 74–78, https://doi.org/10.1016/j.scriptamat.2016.10.035.
[26] K. Kunze, T. Etter, J. Grässlin, V. Shklover, Texture, anisotropy in microstructure and mechanical properties of IN738LC alloy processed by selective laser melting (SLM), Mater. Sci. Eng. A. 620 (2014) 213–222, https://doi.org/10.1016/j.msea.2014.10.003.
[27] N. D'Souza, M. Lekstrom, H.B. Dong, An analysis of measurement of solute segregation in Ni-base superalloys using X-ray spectroscopy, Mater. Sci. Eng. A. 490 (2008) 258–265, https://doi.org/10.1016/j.msea.2008.01.025.
[28] N. El-Bagoury, M. Waly, A. Nofal, Effect of various heat treatment conditions on microstructure of cast polycrystalline IN738LC alloy, Mater. Sci. Eng. A. 487 (2008) 152–161, https://doi.org/10.1016/j.msea.2007.10.004.
[29] M. Mostafaei, S.M. Abbasi, Solutioning and solidification process control in Ta-modified CM247 LC superalloy, J. Mater. Process. Technol. 231 (2016) 113–124, https://doi.org/10.1016/j.jmatprotec.2015.12.021.
[30] A.B. Parsa, P. Wollgramm, H. Buck, C. Somsen, A. Kostka, I. Povstugar, P.-P. Choi, D. Raabe, A. Dlouhy, J. Müller, E. Spiecker, K. Demtroder, J. Schreuer, K. Neuking, G. Eggeler, Advanced scale bridging microstructure analysis of single crystal Ni-base superalloys, Adv. Eng. Mater. 17 (2015) 216–230, https://doi.org/10.1002/adem.201400136.
[31] M.S.A.S. a Karunaratne, D.C.C. Cox, P. Carter, R.C.C. Reed, Modelling of the microsegregation in CMSX-4 superalloy and its homogenisation during heat treatment, in: Superalloys 2000 (Ninth Int. Symp., TMS, 2000, pp. 263–272, https://doi.org/10.7449/2000/Superalloys_2000_263_272.
[32] M. Ramsperger, R.F. Singer, C. Körner, Microstructure of the nickel-base superalloy CMSX-4 fabricated by selective electron beam melting, Metall. Mater. Trans. 47 (2016) 1469–1480, https://doi.org/10.1007/s11661-015-3300-y.
[33] A. Hariharan, L. Lu, J. Risse, A. Kostka, B. Gault, E.A. Jägle, D. Raabe, Misorientation-dependent solute enrichment at interfaces and its contribution to defect formation mechanisms during laser additive manufacturing of superalloys, Phys. Rev. Mater. 3 (2019) 123602, https://doi.org/10.1103/PhysRevMaterials.3.123602.
[34] X. Wang, L.N. Carter, B. Pang, M.M. Attallah, M.H. Loretto, Microstructure and yield strength of SLM-fabricated CM247LC Ni-Superalloy, Acta Mater. 128 (2017) 87–95, https://doi.org/10.1016/j.actamat.2017.02.007.
[35] L. Cui, S. Jiang, J. Xu, R.L. Peng, R.T. Mousavian, J. Moverare, Revealing relationships between microstructure and hardening nature of additively manufactured 316L stainless steel, Mater. Des. 198 (2021) 109385, https://doi.org/10.1016/j.matdes.2020.109385.
[36] Y.M. Wang, T. Voisin, J.T. McKeown, J. Ye, N.P. Calta, Z. Li, Z. Zeng, Y. Zhang, W. Chen, T.T. Roehling, R.T. Ott, M.K. Santala, P.J. Depond, M.J. Matthews, A. V. Hamza, T. Zhu, Additively manufactured hierarchical stainless steels with high strength and ductility, Nat. Mater. 17 (2018) 63–71, https://doi.org/10.1038/nmat5021.
[37] J. Xu, H. Gruber, R. Boyd, S. Jiang, R.L. Peng, J.J. Moverare, On the strengthening and embrittlement mechanisms of an additively manufactured Nickel-base superalloy, Materialia 10 (2020) 100657, https://doi.org/10.1016/j.mtla.2020.100657.
[38] G. Wang, H. Ouyang, C. Fan, Q. Guo, Z. Li, W. Yan, Z. Li, The origin of high-density dislocations in additively manufactured metals, Mater. Res. Lett. 8 (2020) 283–290, https://doi.org/10.1080/21663831.2020.1751739.
[39] M.T.T. Kim, S.Y.Y. Chang, J.B.B. Won, Effect of HIP process on the micro-structural evolution of a nickel-based superalloy, Mater. Sci. Eng. A. 441 (2006) 126–134, https://doi.org/10.1016/j.msea.2006.09.060.
[40] L. Liu, T.W.W. Huang, J. Zhang, H.Z.Z. Fu, Microstructure and stress rupture properties of single crystal superalloy CMSX-2 under high thermal gradient directional solidification, Mater. Lett. 61 (2007) 227–230, https://doi.org/10.1016/j.matlet.2006.04.037.
[41] M. Ramsperger, L. Mújica Roncery, I. Lopez-Galilea, R.F. Singer, W. Theisen, C. Körner, Solution heat treatment of the single crystal nickel-base superalloy CMSX-4 fabricated by selective electron beam melting, Adv. Eng. Mater. 17 (2015) 1486–1493, https://doi.org/10.1002/adem.201500037.
[42] G.E. Fuchs, Solution heat treatment response of a third generation single crystal Ni-base superalloy, Mater. Sci. Eng. A. 300 (2001) 52–60, https://doi.org/10.1016/S0921-5093(00)01776-7.
[43] S.L. Semiatin, F. Zhang, J.S. Tiley, D.U. Furrer, A comparison of the precipitation behavior in PM γ-γ′ nickel-base superalloys, Mater. A. T. High. Temp. 33 (2016) 301–309, https://doi.org/10.1080/09603409.2016.1165449.
[44] I.M. Lifshitz, V.V. Slyozov, The kinetics of precipitation from supersaturated solid solutions, J. Phys. Chem. Solid. 19 (1961) 35–50, https://doi.org/10.1016/0022-3697(61)90054-3.
[45] E.Z. Wagner Cz, Theory of precipitate change by redissolution, Angew Phys Chem 65 (1961) 581–591.
[46] S. Khan, J.B. Singh, A. Verma, Precipitation behaviour of γ′ phase in Alloy 693, Mater. Char. 119 (2016) 24–33, https://doi.org/10.1016/j.matchar.2016.07.007.
[47] K. Chen, R. Huang, Y. Li, S. Lin, W. Zhu, N. Tamura, J. Li, Z. Shan, E. Ma, Rafting-enabled recovery avoids recrystallization in 3D-printing-repaired single-crystal superalloys, Adv. Mater. 32 (2020) 1907164, https://doi.org/10.1002/adma.201907164.
[48] Z. Li, Q. Xu, B. Liu, Microstructure simulation on recrystallization of an as-cast nickel based single crystal superalloy, Comput. Mater. Sci. 107 (2015) 122–133, https://doi.org/10.1016/j.commatsci.2015.05.020.
[49] S.L. Shang, C.L. Zacherl, H.Z. Fang, Y. Wang, Y. Du, Z.K. Liu, Effects of alloying element and temperature on the stacking fault energies of dilute Ni-base superalloys, J. Phys. Condens. Matter 24 (2012) 505403, https://doi.org/10.1088/0953-8984/24/50/505403.
[50] X.-X. Yu, C.-Y. Wang, The effect of alloying elements on the dislocation climbing velocity in Ni: a first-principles study, Acta Mater. 57 (2009) 5914–5920, https://doi.org/10.1016/j.actamat.2009.08.019.
[51] J. Xu, H. Gruber, D. Deng, R.L.R.L. Peng, J.J.J. Moverare, Short-term creep behavior of an additive manufactured non-weldable Nickel-base superalloy evaluated by slow strain rate testing, Acta Mater. 179 (2019) 142–157, https://doi.org/10.1016/j.actamat.2019.08.034.
[52] F. Geiger, K. Kunze, T. Etter, Tailoring the texture of IN738LC processed by selective laser melting (SLM) by specific scanning strategies, Mater. Sci. Eng. A. 661 (2016) 240–246, https://doi.org/10.1016/j.msea.2016.03.036.
[53] O.M.D.M. Messé, R. Muñoz-Moreno, T. Illston, S. Baker, H.J. Stone, Metastable carbides and their impact on recrystallisation in IN738LC processed by selective laser melting, Addit. Manuf. 22 (2018) 394–404, https://doi.org/10.1016/j.addma.2018.05.030.
[54] G. Gottstein, L.S. Shvindlerman, Grain Boundary Migration in Metals, second ed., CRC Press, Boca Raton, 2009 https://doi.org/10.1201/9781420054361.
[55] D.P. Field, L.T. Bradford, M.M. Nowell, T.M. Lillo, The role of annealing twins during recrystallization of Cu, Acta Mater. 55 (2007) 4233–4241, https://doi.org/10.1016/j.actamat.2007.03.021.
[56] R.L. Fullman, J.C. Fisher, formation of annealing twins during grain growth, J. Appl. Phys. 22 (1951) 1350–1355, https://doi.org/10.1063/1.1699865.
[57] V.Y. Gertsman, K. Tangri, R.Z. Valiev, On the grain boundary statistics in metals and alloys susceptible to annealing twinning, Acta Metall. Mater. 42 (1994) 1785–1804, https://doi.org/10.1016/0956-7151(94)90004-3.
[58] Z.G. Zhu, Q.B. Nguyen, F.L. Ng, X.H. An, X.Z. Liao, P.K. Liaw, S.M.L. Nai, J. Wei, Hierarchical microstructure and strengthening mechanisms of a CoCrFeNiMn high entropy alloy additively manufactured by selective laser melting, Scripta Mater. 154 (2018) 20–24, https://doi.org/10.1016/j.scriptamat.2018.05.015.
[59] E.I. Galindo-Nava, L.D. Connor, C.M.F. Rae, On the prediction of the yield stress of unimodal and multimodal γ′ Nickel-base superalloys, Acta Mater. 98 (2015) 377–390, https://doi.org/10.1016/j.actamat.2015.07.048.

Further reading

[1] R.C. Reed, The Superalloys Fundamentals and Applications, Cambridge University Press, Cambridge, 2006.
[2] T.M. Pollock, S. Tin, Nickel-based superalloys for advanced turbine engines: chemistry, microstructure and properties, J. Propul. Power 22 (2006) 361–374, https://doi.org/10.2514/1.18239.
[3] C. Panwisawas, Y.T. Tang, R.C. Reed, Metal 3D printing as a disruptive technology for superalloys, Nat. Commun. 11 (2020), https://doi.org/10.1038/s41467-020-16188-7.